

# Broadband stimulated Raman scattering with Fourier-transform detection

Julien Réhault,<sup>1,2</sup> Francesco Crisafi,<sup>1</sup> Vikas Kumar,<sup>1</sup> Gustavo Ciardi,<sup>1</sup> Marco Marangoni,<sup>1</sup> Giulio Cerullo<sup>1</sup> and Dario Polli<sup>1,\*</sup>

<sup>1</sup>IFN-CNR, Dipartimento di Fisica, Politecnico di Milano, Piazza Leonardo da Vinci 32, 20133, Milano, Italy.

<sup>2</sup>Current address: Paul Scherrer Institute, CH-5232 Villigen PSI, Switzerland

[\\*dario.polli@polimi.it](mailto:dario.polli@polimi.it)

**Abstract:** We propose a new approach to broadband Stimulated Raman Scattering (SRS) spectroscopy and microscopy based on time-domain Fourier transform (FT) detection of the stimulated Raman gain (SRG) spectrum. We generate two phase-locked replicas of the Stokes pulse after the sample using a passive birefringent interferometer and measure by the FT technique both the Stokes and the SRG spectra. Our approach blends the very high sensitivity of single-channel lock-in balanced detection with the spectral coverage and resolution afforded by FT spectroscopy. We demonstrate our method by measuring the SRG spectra of different compounds and performing broadband SRS imaging on inorganic blends.

©2015 Optical Society of America. One print or electronic copy may be made for personal use only. Systematic reproduction and distribution, duplication of any material in this paper for a fee or for commercial purposes, or modifications of the content of this paper are prohibited.

Online abstract in the OSA Journal: <http://dx.doi.org/10.1364/OE.23.025235>

**OCIS codes:** (320.7090) Ultrafast lasers; (290.5910) Scattering, stimulated Raman; (300.6300) Spectroscopy, Fourier transforms.

---

## References and links

1. M. Ghomi, *Applications of Raman Spectroscopy to Biology: from Basic Studies to Disease Diagnosis* (IOS, 2012).
2. H. Kano, H. Segawa, P. Leproux, and V. Couderc, "Linear and nonlinear Raman microspectroscopy: history, instrumentation, and applications," *Opt. Rev.* **21**(6), 752–761 (2014).
3. C. Krafft, B. Dietzek, and J. Popp, "Raman and CARS microspectroscopy of cells and tissues," *Analyst* **134**(6), 1013–1248 (2009).
4. G. Turrell and J. Corset, *Raman Microscopy: Developments and Applications* (Academic, 1996).
5. C. L. Evans, and X. S. Xie, "Coherent anti-stokes Raman scattering microscopy: chemical imaging for biology and medicine," *Annu. Rev. Anal. Chem.* **1**(1), 883–909 (2008).
6. A. Zumbusch, G. R. Holtom, and X. S. Xie, "Three-dimensional vibrational imaging by coherent anti-Stokes Raman scattering," *Phys. Rev. Lett.* **82**(20), 4142–4145 (1999).
7. Ch. W. Freudiger, W. Min, B. G. Saar, S. Lu, G. R. Holtom, C. He, J. C. Tsai, J. X. Kang, and X. S. Xie, "Label-free biomedical imaging with high sensitivity by stimulated Raman scattering microscopy," *Science* **322**(5909), 1857–1861 (2008).
8. P. Nandakumar, A. Kovalev, and A. Volkmer, "Vibrational imaging based on stimulated Raman scattering microscopy," *New J. Phys.* **11**, 033026 (2009).
9. C. L. Evans, E. O. Potma, M. Puoris'haag, D. Cote, C. P. Lin, and X. S. Xie, "Chemical imaging of tissue *in vivo* with video-rate coherent anti-Stokes Raman scattering microscopy," *Proc. Natl. Acad. Sci. USA* **102**(46), 16807–16812 (2005).
10. B. G. Saar, C. W. Freudiger, J. Reichman, C. M. Stanley, G. R. Holtom, and X. S. Xie, "Video-rate molecular imaging *in vivo* with stimulated Raman scattering," *Science* **330**(6009), 1368–1370 (2010).
11. T. W. Kee, and M. T. Cicerone, "Simple approach to one-laser, broadband coherent anti-Stokes Raman scattering microscopy," *Opt. Lett.* **29**(23), 2701–2703 (2004).
12. H. Kano, and H. Hamaguchi, "Ultrabroadband (>2500 cm<sup>-1</sup>) multiplex coherent anti-Stokes Raman scattering microspectroscopy using a supercontinuum generated from a photonic crystal fiber," *Appl. Phys. Lett.* **86**(12), 121113 (2005).

13. B. von Vacano, L. Meyer, and M. Motzkus, "Rapid polymer blend imaging with quantitative broadband multiplex CARS microscopy," *J. Raman Spectrosc.* **38**(7), 916–926 (2007).
14. R. Selm, M. Winterhalder, A. Zumbusch, G. Krauss, T. Hanke, A. Sell, and A. Leitenstorfer, "Ultrabroadband background-free coherent anti-Stokes Raman scattering microscopy based on a compact Er: fiber laser system," *Opt. Lett.* **35**(19), 3282–3284 (2010).
15. C. H. Camp Jr, Y. J. Lee, J. M. Heddleston, Ch. M. Hartshorn, A. R. Hight Walker, J. N. Rich, J. D. Lathia, and M. T. Cicerone, "High-speed coherent Raman fingerprint imaging of biological tissues," *Nature Photon.* **8**(8), 627–634 (2014).
16. J. P. Ogilvie, E. Beaurepaire, A. Alexandrou, and M. Joffe, "Fourier-transform coherent anti-Stokes Raman scattering microscopy," *Opt. Lett.* **31**(4), 480–482 (2006).
17. T. Ideguchi, S. Holzner, B. Bernhardt, G. Guelachvili, N. Picqué, and T. W. Hänsch, "Coherent Raman spectro-imaging with laser frequency combs," *Nature* **502**(7471), 355–358 (2013).
18. M. T. Cicerone, K. A. Aamer, Y. J. Lee, and E. Vartiainen, "Maximum entropy and time-domain Kramers–Kronig phase retrieval approaches are functionally equivalent for CARS microspectroscopy," *J. Raman Spectrosc.* **43**(5), 637–643 (2012).
19. Y. Liu, Y. J. Lee, and M. T. Cicerone, "Broadband CARS spectral phase retrieval using a time-domain Kramers–Kronig transform," *Opt. Lett.* **34**(9), 1363–1365 (2009).
20. L. Kong, M. Ji, G. R. Holtom, D. Fu, C. W. Freudiger, and X. Sunney Xie, "Multicolor stimulated Raman scattering microscopy with a rapidly tunable optical parametric oscillator," *Opt. Lett.* **38**(2), 145–147 (2013).
21. Y. Ozeki, W. Umemura, Y. Otsuka, S. Satoh, H. Hashimoto, K. Sumimura, N. Nishizawa, K. Fukui, and K. Itoh, "High-speed molecular spectral imaging of tissue with stimulated Raman scattering," *Nat. Photon.* **6**(12), 845–851 (2012).
22. S. Karpf, M. Eibl, W. Wieser, T. Klein, and R. Huber, "A time-encoded technique for fibre-based hyperspectral broadband stimulated Raman microscopy," *Nat. Commun.* **6**, 6784 (2015).
23. K. Seto, Y. Okuda, E. Tokunaga, and T. Kobayashi, "Development of a multiplex stimulated Raman microscope for spectral imaging through multi-channel lock-in detection," *Rev. Sci. Instrum.* **84**(8), 083705 (2013).
24. K. Seto, Y. Okuda, E. Tokunaga, and T. Kobayashi, "Multiplex stimulated Raman imaging with white probe-light from a photonic-crystal fibre and with multi-wavelength balanced detection," *J. Phys. D* **47**(34), 34540 (2014).
25. C.-S. Liao, M. N. Slipchenko, P. Wang, J. Li, S.-Y. Lee, R. A. Oglesbee, and J.-X. Cheng, "Microsecond scale vibrational spectroscopic imaging by multiplex stimulated Raman scattering microscopy," *Light Sci. Appl.* **4**, e265 (2015).
26. E. Ploetz, S. Laimgruber, S. Berner, W. Zinth, and P. Gilch, "Femtosecond stimulated Raman microscopy," *Appl. Phys. B* **87**(3), 389–393 (2007).
27. E. Ploetz, B. Marx, T. Klein, R. Huber, and P. Gilch, "A 75 MHz light source for femtosecond stimulated Raman microscopy," *Opt. Expr.* **17**(21), 18612–18620 (2009).
28. W. Rock, M. Bonn, and S. H. Parekh, "Near shot-noise limited hyperspectral stimulated Raman scattering spectroscopy using low energy lasers and a fast CMOS array," *Opt. Expr.* **21**(13), 15113–15120 (2013).
29. D. Fu, F.-K. Lu, X. Zhang, C. Freudiger, D.R. Pernik, G. Holtom, and X. S. Xie, "Quantitative chemical imaging with multiplex stimulated Raman scattering microscopy," *J. Am. Chem. Soc.* **134**(8), 3623–3626 (2012).
30. T. Hellerer, A. M. K. Enejder, and A. Zumbusch, "Spectral focusing: High spectral resolution spectroscopy with broad-bandwidth laser pulses," *Appl. Phys. Lett.* **85**(1), 25–27 (2004).
31. D. Fu, G. Holtom, C. Freudiger, X. Zhang, and X. S. Xie, "Hyperspectral imaging with stimulated Raman scattering by chirped femtosecond lasers," *J. Phys. Chem. B* **117**(16), 4634–4640 (2013).
32. E. R. Andresen, P. Berto, and H. Rigneault, "Stimulated Raman scattering microscopy by spectral focusing and fiber-generated soliton as Stokes pulse," *Opt. Lett.* **36**(13), 2387–2389 (2011).
33. W. J. Jones, and B. P. Stoicheff, "Inverse Raman spectra: induced absorption at optical frequencies," *Phys. Rev. Lett.* **13**(22), 657–659 (1964).
34. S. P. Davis, M. C. Abrams and J. W. Brault, *Fourier Transform Spectrometry* (Elsevier 2001).
35. M. Marangoni, A. Gambetta, C. Manzoni, V. Kumar, R. Ramponi, and G. Cerullo, "Fiber-format CARS spectroscopy by spectral compression of femtosecond pulses from a single laser oscillator," *Opt. Lett.* **34**(21), 3262–3264 (2009).
36. G. Krauss, T. Hanke, A. Sell, D. Träutlein, A. Leitenstorfer, R. Selm, M. Winterhalder, and A. Zumbusch, "Compact coherent anti-Stokes Raman scattering microscope based on a picosecond two-color Er: fiber laser system," *Opt. Lett.* **34**(18), 2847–2849 (2009).
37. D. Brida, C. Manzoni, and G. Cerullo, "Phase-locked pulses for two-dimensional spectroscopy by a birefringent delay line," *Opt. Lett.* **37**(15), 3027–3029 (2012).
38. J. Réhault, M. Maiuri, A. Oriana, and G. Cerullo, "Two-dimensional electronic spectroscopy with birefringent wedges," *Rev. Sci. Instrum.* **85**(12), 123107 (2014).
39. J. Réhault, M. Maiuri, C. Manzoni, D. Brida, J. Helbing, and G. Cerullo, "2D IR spectroscopy with phase-locked pulse pairs from a birefringent delay line," *Opt. Express* **22**(8), 9063–9072 (2014).

40. A. Gambetta, V. Kumar, G. Grancini, D. Polli, R. Ramponi, G. Cerullo, and M. Marangoni, "Fiber-format stimulated-Raman-scattering microscopy from a single laser oscillator," *Opt. Lett.* **35**(2), 226–228 (2010).
  41. K. Nose, Y. Ozeki, T. Kishi, K. Sumimura, N. Nishizawa, K. Fukui, Y. Kanematsu, and K. Itoh, "Sensitivity enhancement of fiber-laser-based stimulated Raman scattering microscopy by collinear balanced detection technique," *Opt. Express* **20**(13), 13958–13965 (2012).
  42. Ch.W. Freudiger, W. Yang, G.R. Holtom, N. Peyghambarian, X. S. Xie, and K.Q. Kieu, "Stimulated Raman scattering microscopy with a robust fibre laser source," *Nature Photon.* **8**(2), 153–159 (2014).
  43. J. Jaumot, R. Gargallo, A. de Juan, and R. Tauler, "A graphical user-friendly interface for MCR-ALS: a new tool for multivariate curve resolution in MATLAB," *Chemom. Intell. Lab. Syst.* **76**(1), 101–110 (2005).
  44. P. B. Felgett, "On the ultimate sensitivity and practical performance of radiation detectors," *J. Opt. Soc. Am.* **39**(11), 970–976 (1939).
  45. J. F. de Boer, B. Cense, B. H. Park, M. C. Pierce, G. J. Tearney, and B. E. Bouma, "Improved signal-to-noise ratio in spectral-domain compared with time-domain optical coherence tomography," *Opt. Lett.* **28**(21), 2067–2069 (2003).
  46. R. Leitgeb, C. K. Hitzenberger, and A. F. Fercher "Performance of fourier domain vs. time domain optical coherence tomography," *Opt. Expr.* **11**(8), 889–894 (2003).
- 

## 1. Introduction

Raman microscopy is gaining increasing recognition in biomedical optics [1] due to its capability of non-invasive, label-free imaging of tissues and cells, based on their intrinsic vibrational response [2,3]. In spontaneous Raman (SR) [4] a quasi-monochromatic laser at frequency  $\omega_p$  ("pump") excites the molecule to a virtual state, which then relaxes to the ground state emitting photons at lower frequencies  $\omega_s$  ("Stokes"). The inelastic frequency shifts  $\Omega = \omega_p - \omega_s$  match the molecular vibrations and the resulting vibrational spectrum reflects the molecular structure, providing a detailed picture of the biochemical composition of the specimen. The main drawback of SR is its very weak scattering cross section, 10-12 orders of magnitude lower than that of absorption. This makes it difficult to separate the weak Raman-shifted light from the intense elastic scattering and from sample and substrate fluorescence, preventing probing dilute species and *in vivo* imaging, due to the long integration times needed.

Coherent Raman Scattering (CRS) [5] can overcome these limitations, exploiting the third-order nonlinear optical response of the sample to pump and Stokes pulses in order to set up and detect a vibrational coherence within the ensemble of molecules inside the laser focus. When the difference between pump and Stokes frequencies matches a characteristic vibrational frequency  $\Omega$ , i.e.  $\omega_p - \omega_s = \Omega$ , then all the molecules in the focal volume are resonantly excited and vibrate in phase; this vibrational coherence enhances the Raman response by many orders of magnitude with respect to the incoherent SR process. The two most widely employed CRS techniques are Coherent Anti-Stokes Raman Scattering (CARS) [6] and Stimulated Raman Scattering (SRS) [7,8]. CARS detects the coherent radiation at the anti-Stokes (blue-shifted) frequency  $\omega_{as} = \omega_p + \Omega$ . SRS monitors either the stimulated emission of Stokes photons from a virtual state of the sample to the investigated vibrational state (the so-called Stimulated Raman Gain, SRG) or the absorption of pump photons from the ground state (Stimulated Raman Loss, SRL). CARS and SRS have both advantages and drawbacks and are actively developed for high-speed vibrational imaging.

State-of-the-art CRS microscopy has reached extremely high imaging speed (up to the video rate [9,10]), but working only at one vibrational frequency (single-color CRS). This provides limited chemical selectivity in complex heterogeneous systems, such as cells and tissues, with spectrally overlapping chemical species. Broadband CRS microscopy has been so far mostly implemented in the CARS configuration [11-17]. In this method, an ultra-broadband laser pulse, or a combination of two properly detuned pump and Stokes pulses, first create the vibrational coherence in the sample. A narrowband pulse then probes the coherence by transferring the vibrational spectrum to the blue-shifted anti-Stokes region, thus in the absence of any linear background light, enabling direct signal detection by photon counting. Despite this advantage, CARS suffers from the so-called non-resonant background (NRB) caused by the

purely electronic third-order nonlinear response of the molecules or the medium in which they are embedded, i.e. not mediated by any characteristic vibration of the sample. NRB may strongly distort or even overwhelm the molecular vibrational spectrum of interest. The extraction of quantitative information from these altered spectra requires the application of complex phase-retrieval algorithms [15,18]. Furthermore, since the CARS signal is homodyne detected, it scales quadratically with the number of oscillators in the focal volume, making it hard to perform quantitative measurements and to probe dilute species. This problem can be alleviated by exploiting the NRB as a phase-locked local oscillator, allowing to perform heterodyne detection and to recover the linear concentration dependence [15, 19].

SRS does not suffer from NRB and, since the signal is heterodyne detected, it inherently provides a linear dependence of the signal on the sample concentration; however, its extension to the broadband modality is technically challenging. SRS in fact requires the detection of a very small differential signal (SRG/SRL) on top of the intense Stokes/pump pulse, which is only possible through sensitive modulation transfer schemes. To achieve high-speed imaging by SRS, the detection chain needs to be carefully designed to provide sensitivity levels close to the shot noise limit. In the single-color regime this is typically accomplished by high-frequency amplitude modulation of one of the laser beams (pump or Stokes) followed by lock-in detection of its counterpart (Stokes or pump). Extension of this approach to a broadband configuration would require a multichannel high-frequency lock-in amplifier, which is not readily available.

Only a few experimental demonstrations of broadband SRS microscopy have been presented so far. A first approach is based on narrowband pump and Stokes pulses and single-color detection. Either the pump or the Stokes spectrum is kept fixed, while the other is rapidly tuned via a picosecond optical parametric oscillator and an electro-optical tunable Lyot filter [20] or using two synchronized laser sources and a wavelength scanner in a 4-f scheme [21]. For every corresponding Raman frequency, the sample is raster scanned either line-by-line or frame-by-frame and multispectral images are finally reconstructed by stacking the data. The achieved tuning range is however narrow ( $\sim 300\text{ cm}^{-1}$ ) due to the limited achievable tuning range/bandwidth of the laser. Another somewhat similar approach has also been recently demonstrated using a time-encoded method [22]. It has the advantages of high spectral resolution (better than  $3\text{ cm}^{-1}$ ) and large spectral coverage ( $600\text{-cm}^{-1}$  for a single laser configuration and gap-free from  $250$  to  $3150\text{ cm}^{-1}$  combining four different lasers), but at the expense of using continuous-wave lasers with low power densities which limit the SRS signal amplitude.

A second approach to broadband SRS involves the use of a broadband Stokes (pump) pulse combined with multichannel detection. This approach is conceptually very powerful as it avoids frequency tuning and enables parallel detection of all frequencies, but poses the technical challenge of developing a multichannel detection with the speed and sensitivity required for SRS. Among the proposed experimental schemes, a first group employs an array of photodetectors, each one connected to a specific input port of a multi-channel lock-in amplifier [23,24] This solution is extremely powerful, but it requires a complex and costly dedicated electronics, making it difficult to translate it to mainstream biomedical applications. A recently proposed approach, which is much simpler yet very effective, involves the use of an array of tuned LC filters [25]. An alternative scheme makes use of a spectrometer equipped with a CCD/CMOS/NMOS linear image sensor [26-28]. This solution is mainly limited by the full-well capacity of the pixels, of the order of  $10^6$  electrons, which reduces the achievable signal-to-noise ratio to  $\Delta I_S/I_S \geq 10^{-3}$  for a single spectrum (depending on the number of photons illuminating each pixel). As the read-out speed typically cannot exceed a few kilohertz, it would require several seconds or even minutes to achieve a sensitivity down to  $\Delta I_S/I_S = 10^{-5}$ , needed for most applications. A third method is based on the modulation of different spectral portions of the broadband pulse at different frequencies using an acousto-optical tunable filter device, so that the different Raman lines can be measured simultaneously and distinguished by demodulating the signal at different frequencies [29]. Finally, spectral focusing [30] of

broadband pump/Stokes pulses in combination with rapid variations of their delay can be used [31,32].

In this paper, we propose and demonstrate a new approach to broadband SRS based on time-domain Fourier transform (FT) detection of the SRG spectrum. We use a passive birefringent delay line that guarantees exceptional ( $<\lambda/300$ ) path-length stability and reproducibility for time-domain detection of the broadband Stokes pulse. We further exploit the linearity of the FT operator for time-domain measurement of the SRG spectrum by high-frequency modulation of the pump and single-channel, lock-in detection. Our approach conjugates the very high sensitivity of single-channel lock-in detection with the spectral resolution afforded by FT spectroscopy. We demonstrate our method by measuring broadband SRS spectra of different compounds and performing broadband SRS imaging of polymer blends.

## 2. Principle of Fourier transform SRS

In order to understand the principle of our broadband FT-SRS, let us compare it with standard multichannel SRS detection, the conceptual scheme of which is shown in Fig. 1(a). For the case of SRG detection, a narrowband pump pulse and a broadband Stokes are synchronized, collinearly combined by a dichroic beam splitter and focused on the sample. The intensity of the pump beam is modulated at high frequency, ideally at half the repetition rate of the laser. Modulation transfer to the broadband Stokes pulse occurs at the frequencies where SRG takes place, due to the presence of specific molecular vibrations. After the sample (in the case of a measurement in transmission), a filter rejects the pump photons and the Stokes spectrum is detected using the aforementioned multi-channel scheme based on, e.g., a photodiode array and a multi-channel lock-in amplifier (Fig. 1(a), gray box named (a1)) [23,24] or a tuned amplifier [25]. It is also possible to combine a broadband pump with a narrowband Stokes and measure the SRL of the pump, in a process known as Inverse Raman scattering [33].

Our approach (see Fig. 1(a), gray box named (a2)) is radically different, as it requires a single photodetector and a single-channel lock-in amplifier. It makes use of the time-domain measurement of spectra enabled by FT spectroscopy, in analogy with the FTIR technique used in the mid-infrared region [34]. The Stokes pulse after the sample is sent to a linear interferometer (e.g. a Michelson) that creates two *collinear* identical replicas of the pulse, with relative delay  $\tau$ . The two replicas are made to interfere as a function of  $\tau$  onto a single detector, giving rise to an interferogram as that sketched in red in Fig. 1(b). In the following, we will call it “Stokes interferogram”. The FT of the interferogram with respect to  $\tau$  gives the spectrum of the Stokes pulse. The presence of SRG on the Stokes, induced by the pump pulse in a sample with Raman gain, modifies the interferogram (see Fig. 1(b)) generating tails at long delays. Its FT results in a different Stokes spectrum, as it now displays gain in the form of sharp peaks at specific Stokes shifts. In Fig. 1(b), the gain is exaggerated, to highlight the concept, but in practical conditions the differences between the two interferograms and between the two Stokes spectra are as low as a few parts in  $10^4$  or  $10^5$ . By computing the difference of the two Stokes spectra and normalizing over the Stokes spectrum one obtains the SRG spectrum.

For long delays the difference between the two red interferograms in Fig. 1(b) is immediately visible because, in the presence of the pump, the interferogram shows persistent oscillations that are not present without it. This is due to the fact that molecular vibrations have coherence times of the order of a few picoseconds, much longer than the Stokes pulse duration ( $\approx 20$ fs in our case), so that they manifest in the time domain as oscillations that persist long after the Stokes interferogram has decayed. In the spectral domain, due to the well-known time-frequency reciprocity, this results in narrow linewidths (few tens of wavenumbers, to be compared with the Stokes linewidth of  $\approx 700$   $\text{cm}^{-1}$  FWHM in our case).

To measure the tiny pump-induced modification of the Stokes signal, we implement high-speed modulation transfer and lock-in detection. Thanks to the linearity of the FT operator, the difference between the FTs of two signals (see Fig. 1(b), upper part) is equal to the FT of the

difference of the two signals (see Fig. 1(b), lower part). In our case, the signals are the interferograms and their FTs are the corresponding spectra. We take advantage of this property, by first obtaining directly the difference of the two Stokes pulse interferograms using a lock-in amplifier, resulting in the blue interferogram in Fig. 1(b), called “SRS interferogram” in the following. Secondly, we calculate the FT of the SRS interferogram to finally obtain the SRS spectrum.

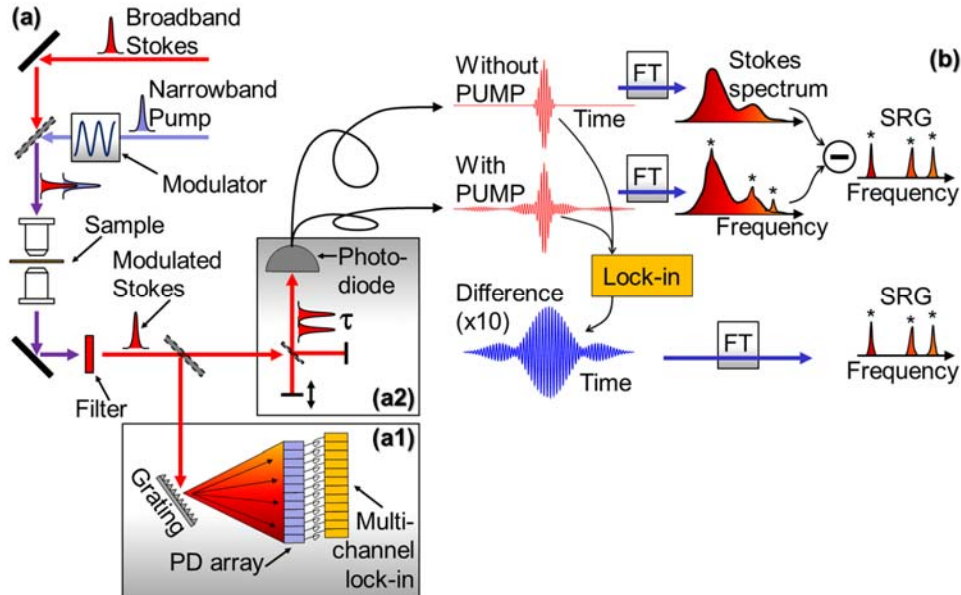


Fig. 1. (a) Experimental setup for multiplex SRS with two different detection schemes: (a1) multi-channel detection, based on a dispersive element such as a grating; (a2) FT detection, based on an interferometer. (b) Conceptual scheme for FT-SRS: to measure the SRG spectrum, instead of computing the difference of the two Stokes spectra (with and without the pump), we first obtain the difference of the two interferograms (with and without the pump) using a lock-in amplifier and then we calculate the FT of the SRS interferogram.

### 3. Experimental setup

The experimental set-up used for broadband FT-SRS is shown in Fig. 2. The excitation system (FemtoFiber Pro from Toptica Photonics) starts with an Er: fiber oscillator feeding two independent Er-doped fiber amplifiers (EDFAs), each producing 70-fs pulses at 1560 nm with 350-mW average power at 40-MHz repetition rate. One EDFA output is frequency doubled in a 1-cm long periodically poled lithium niobate crystal, producing a narrowband ( $\sim 15 \text{ cm}^{-1}$ ) 783-nm pump pulse with average power up to 110 mW and  $\sim 2$ ps duration [35,36]. The second EDFA output is spectrally broadened in a highly nonlinear fiber with a zero dispersion wavelength that is close to, but slightly shorter than, the input laser wavelength. The short-wavelength dispersive wave, peaked at 1050 nm and compressed to nearly transform-limited  $\approx 20$ -25 duration by a SF10 prism pair, is used as the broadband Stokes pulse. Pump and Stokes are synchronized by a delay line, collinearly combined by a dichroic beam splitter and focused onto the sample by a microscope objective. The pump pulse is acousto-optically modulated at 3-MHz frequency with  $\approx 80\%$  diffraction efficiency. After the sample, the Stokes is recollimated by a second objective, filtered from the pump by a long-wave pass filter and sent to a common-mode birefringent interferometer.

The FT procedure requires interferometric stability of the delay between the pulse replicas (or at least interferometric precision in the determination of the phase between the two arms) in order to precisely map the interferogram that oscillates with the optical carrier frequency. To this purpose, we implemented FT-SRS using a recently introduced birefringent interferometer called Translating-Wedge-based Identical pulses eNcoding System (TWINS) [37-39]. It is a passive delay line capable of generating two pulse replicas with attosecond control of their relative delay, thanks to its common-path geometry. The energy of the input beam is equally distributed into two perpendicularly polarized components that collinearly propagate along the fast and slow axes of the birefringent material. The delay between these two components can be arbitrarily controlled varying the thickness of birefringent material, inserting the wedges in and out of the beam through a motorized translation stage.

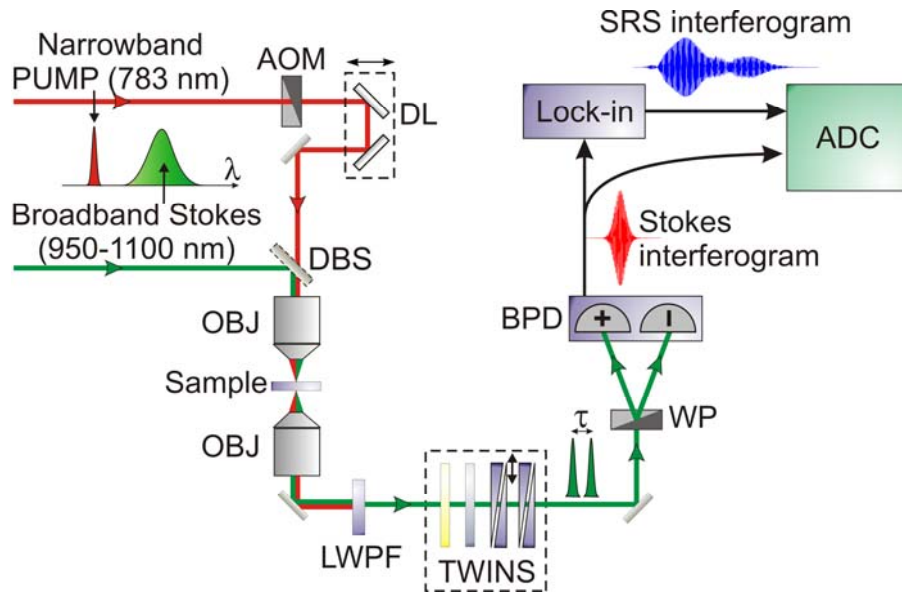


Fig. 2: Experimental setup for FT-SRS. AOM: Acousto-Optic Modulator. DL: Delay Line. OBJ are objectives. DBS: Dichroic beam splitter. LWPF: Long-Wave Pass Filter. TWINS: see text. WP: Wollaston Polarizer. BPD: Balanced photodiodes. ADC: Analog to Digital Converter.

In the standard TWINS configuration, a polarizer at the output projects the two replicas into a common polarization state (at  $45^\circ$  with respect to the two orthogonal polarization directions), to observe their interference. Here we use a Wollaston prism (WP) oriented at  $45^\circ$  with respect to the optical axis of the birefringent wedges. In this way, two spatially separated and perpendicularly polarized beams are generated. Each beam contains the two interfering delayed pulses generated by the TWINS. These two beams are sent to the photodiodes of a balanced detector, which measure two interferograms that are  $180^\circ$  out of phase, due to energy conservation. The output of the balanced detector is sent both to an analog to digital converter (to record the Stokes interferogram) and to a high-frequency lock-in amplifier (to record the SRS interferogram). Since the output of the balanced detector is the difference of the light intensities at the two photodiodes, the interference pattern is multiplied by two with respect to the single-channel configuration. Furthermore, differential detection effectively cancels the Stokes pulse intensity noise for delays longer than  $\approx 80$  fs (i.e. when the Stokes replicas do not interfere anymore so that the two channels are indeed balanced). This balanced detection [40-42] is extremely useful to measure with high signal-to-noise ratio the weak SRS interferogram (which extends much longer in time, up to  $\sim 1$  ps) sitting on the intense Stokes background. It is here straightforwardly implemented in our detection chain, avoiding complications such as

auto-balanced detection [42] or collinear balanced detection [41] that were previously necessary in SRS microscopy.

The FT-SRS measurement is performed translating the wedges at constant speed without any feedback control on the position of the motor during the movement [38]. We verified that no significant deviation from linearity is present in the data by acquiring an interferogram of a cw Helium-Neon laser. In this way, the data collection can be set at constant sampling rate with no delay imposed by any feedback loop. Calibration can be performed either on the Stokes pulse with the help of narrowband interference filters or by measuring the FT-SRS spectrum of reference compounds.

#### 4. Results

Figure 3 reports broadband FT-SRS measurements on isopropanol contained in a cuvette with 1-mm optical path. A couple of 0.3-NA microscope objectives are used for focusing and collection. The Stokes interferogram is displayed in Fig. 3(a) as a red solid curve and the SRS interferogram is plotted in Fig. 3(b) as a blue solid curve as a function of the delay imposed by the TWINS to the two Stokes replicas. We apply a numerical bandpass filter centered at the carrier frequency of the Stokes pulse to both interferograms to remove excess noise. In the inset of Fig 3(b) (gray area), we plot a zoom of the SRS interferogram, to demonstrate that we carefully sample its oscillatory pattern well above the Nyquist limit. Note that, while the Stokes interferogram has a vanishing oscillatory pattern at delays longer than  $\sim 80$  fs (i.e. about 4 times the FWHM transform-limited duration of the Stokes pulse), the SRS interferogram displays strong signal up to hundreds of femtoseconds, as we discussed in Section 2. The SRS interferogram is also symmetric around time zero, but we limit our measurement to a single side of it because, with our wedge size, the maximum delay achievable by TWINS amounts to  $\approx 1$  ps, and this affords a better spectral resolution for the same scan length. This choice, however, is not a fundamental limitation and has the benefit of reducing the total measurement time. Since the balanced detection works effectively only when the Stokes interferogram has decayed to zero, we apply a numerical Gaussian window to the SRS interferogram in order to suppress its initial part.

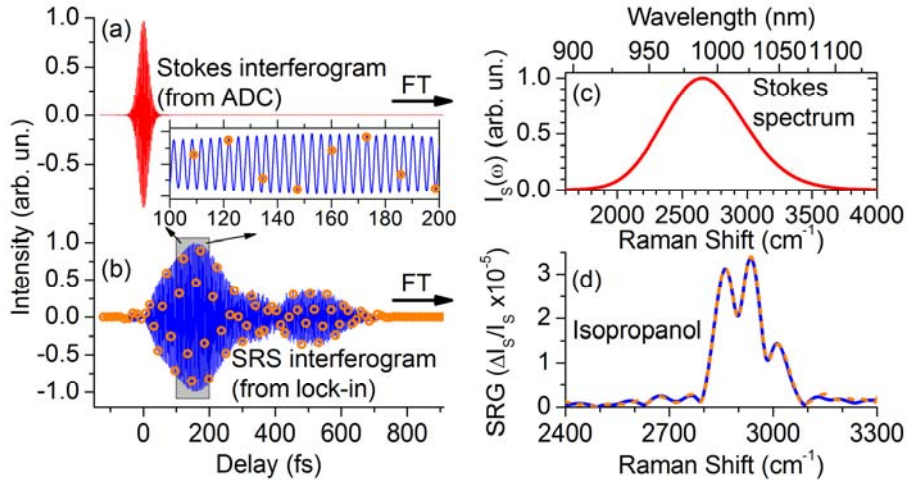


Fig. 3: (a) Stokes interferogram; (b) blue solid curve: SRS interferogram in isopropanol, demodulated by the lock-in amplifier and filtered using a Gaussian window, orange circles: undersampled SRS interferogram; inset: zoom of the interferograms in the 100-200 fs region. (c) spectrum of the Stokes pulse, obtained by considering the absolute value of the FT of (a); (d) SRG spectra of methanol, obtained by normalizing the absolute value of the FT of (b) by the Stokes spectrum, both in the case of the densely sampled interferogram (blue solid curve) and the undersampled one (orange dashed curve).



The Stokes spectrum  $I_S(\omega)$  is calculated by FT of the Stokes interferogram and is plotted in Fig. 3(c) as a function of its Raman shift with respect to the 783-nm pump pulse in order to highlight the Raman spectral coverage of our setup, which amounts to  $\approx 2000 \text{ cm}^{-1}$ . Figure 3(d) reports the SRS spectrum  $\Delta I_S/I_S(\omega)$  of isopropanol as a blue solid curve, calculated by normalizing the FT of the SRS interferogram, corresponding to  $\Delta I_S(\omega)$ , to the Stokes spectrum  $I_S(\omega)$  and taking into account a conversion factor equal to the employed input/output lock-in sensitivity. We note the presence of three clearly distinguished peaks at the vibrational frequencies 2870, 2930 and 3000  $\text{cm}^{-1}$ , corresponding to the  $\text{CH}_3$  symmetric stretch (at 2885  $\text{cm}^{-1}$ ), the CH stretch (at 2920  $\text{cm}^{-1}$ ) and the  $\text{CH}_3$  asymmetric stretches (at 2950 and 2980  $\text{cm}^{-1}$ ) of isopropanol. The integration time of the lock-in was set to 1 ms, which limits the maximum translation speed of the wedges to  $\sim 8 \text{ mm/s}$  to guarantee sufficient sampling of the oscillation pattern. Considering that the overall  $\sim 1$ -ps scan range (see Fig. 3(b)) corresponds to  $\sim 20 \text{ mm}$  lateral scan of the TWINS, it results in almost 3 seconds measurement time for a broadband SRS spectrum. Our spectral resolution is of the order of 30  $\text{cm}^{-1}$ , limited by the scan range of the wedges, but could be easily improved, if required by the experiment, using a different TWINS design, till the 15  $\text{cm}^{-1}$  limit set by the pump pulse bandwidth, at the expense of an increased acquisition time. Using 6-mW pump power and 3.5-mW Stokes power, the resulting maximum SRG signal is of the order of  $\Delta I_S/I_S \sim 3 \cdot 10^{-5}$ . Figure 4 reports similar results on other solvents such as tetrahydrofuran (THF), methanol, and acetone, and on a polymethyl methacrylate (PMMA) film, showing clean peaks which are in agreement with known Raman spectra of the compounds.

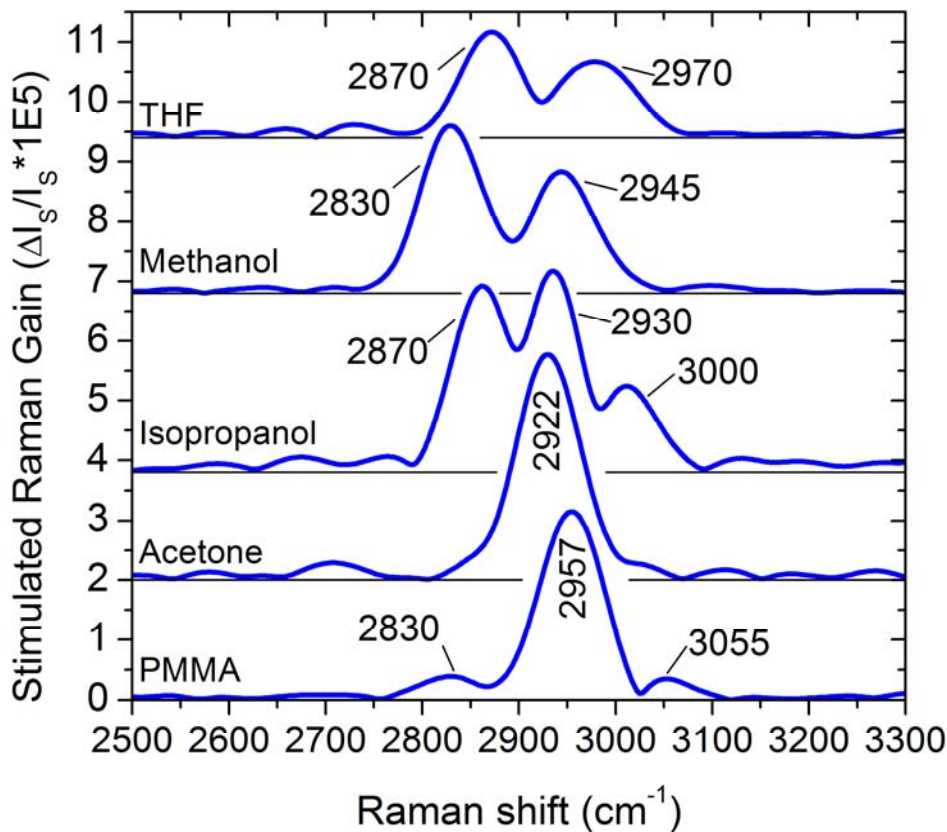


Fig. 4: Broadband SRS spectra of different solvents and a PMMA film measured with the FT technique.

We coupled our FT-SRS detection system to a homemade microscope to perform broadband SRS imaging. We measured a mixture of PMMA and polystyrene (PS) spherical beads with 6- $\mu\text{m}$  and 3- $\mu\text{m}$  diameter, respectively, dispersed on a glass substrate. The sample is mounted on an x-y-z piezo stage with sub-nanometer positioning precision. For these measurements we used two air-corrected 100x 0.75-NA objectives for both focusing and collection, resulting in a spatial resolution that is better than 1  $\mu\text{m}$ . Pump and Stokes power at the sample were 2.5mW and 1.7mW, respectively. Figure 5 reports the results. The imaged area has 21x21  $\mu\text{m}^2$  size and was sampled using 140x140 pixels. The measured three-dimensional dataset as a function of sample position and Raman shift can be decomposed in a series of images at various fixed vibrational frequencies. Figures 5(a)-5(c) report three of them at 2910, 2956 and 3066  $\text{cm}^{-1}$  Raman shifts, while the complete dataset can be seen in the Supplementary Information (see Visualization 1) in the form of a movie in which the vibrational frequency is swept over time.

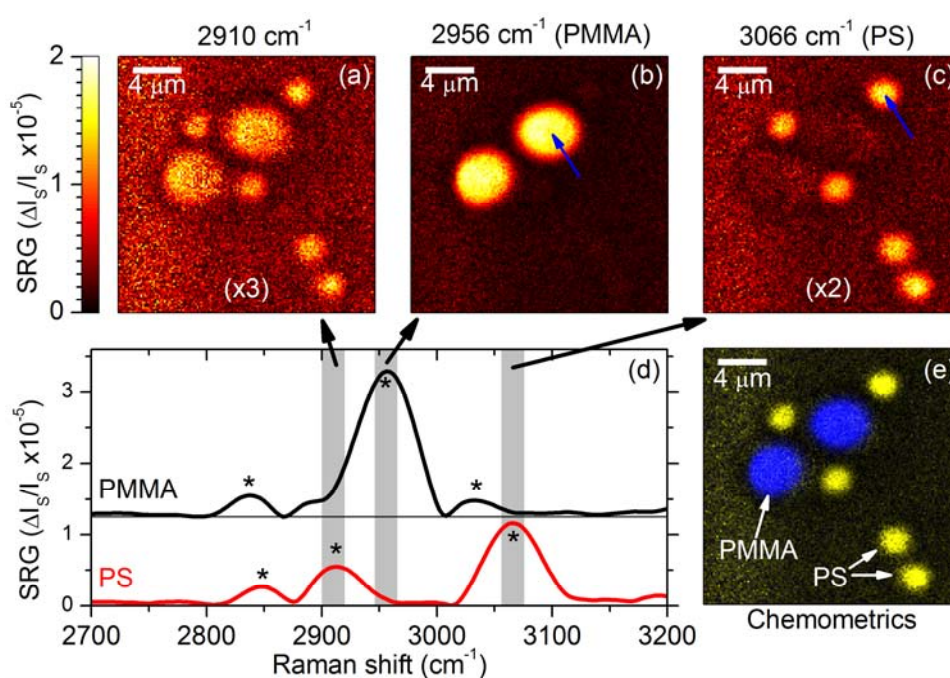


Fig. 5: (a)-(c) Microscopic images of a mixture of 6- $\mu\text{m}$  PMMA beads and 3- $\mu\text{m}$  PS beads collected at different Raman frequencies: 2910  $\text{cm}^{-1}$  (a) in partial resonance with both materials, 2956  $\text{cm}^{-1}$  (b) in resonance with the PMMA beads, and 3066  $\text{cm}^{-1}$  (c) in resonance with the PS beads. See Visualization 1 in the Supplementary Materials online for a movie of the entire sample response. (d) Broadband SRG spectra collected in the center of a PMMA bead (upper black curve) and of a PS bead (lower red curve). Six stars indicate the proper identification of the three characteristic Raman peaks of both PMMA and of PS present in this high-frequency CH stretching region. Gray areas indicate the three spectral regions selected to plot the three images in panels (a)-(c). (e) Overlay image of PMMA (blue) and PS (yellow) concentrations obtained using multivariate statistical analysis.

In the image collected at Raman shift of 2956  $\text{cm}^{-1}$  (Fig. 5(b)) one can clearly recognize two 6- $\mu\text{m}$ -diameter PMMA beads. Figure 5(d) reports as a black solid line the entire Raman spectrum in the 2700-3200  $\text{cm}^{-1}$  vibrational window measured in the center of one of these beads (see blue arrow in Fig. 5(b)). It presents three clear Raman lines, as highlighted with

small stars in Fig. 5(d), corresponding to the well-known signatures of PMMA. Five smaller 3- $\mu\text{m}$ -diameter PS beads are visible in the image collected at 3066  $\text{cm}^{-1}$  Raman shift (Fig. 5(c)). Figure 5(d) reports as a red solid line the corresponding Raman spectrum in the 2700-3200  $\text{cm}^{-1}$  vibrational window, as measured in the center of one of these five beads (see blue arrow in Fig. 5(c)). It exhibits three clear Raman lines, as highlighted with small stars, corresponding to the well-known signatures of PS in this wavenumber region. Finally, Fig. 5(a) reports the image collected at a 2910  $\text{cm}^{-1}$  Raman shift, where both materials display a weak Raman response so that it is possible to see their relative position. Note that single-color SRS, if tuned to this Raman line, would allow detecting both PMMA and PS beads without the possibility of discriminating one from the other (unless making use of their different size in this particular case).

We analyzed our three-dimensional dataset using a Multivariate Curve Resolution-Alternating Least Square (MCR-ALS) algorithm [43] in Matlab. This tool decomposes the experimental dataset in a set of spectra and concentration vectors whose product gives the best fitting to the data matrix [3,21,25]. In our case, it correctly identified two principal components only, with spectra perfectly matching those of PMMA and PS reported in Fig. 5(d). Figure 5(e) reports the corresponding concentration of the two components and provides a clear chemically selective map of the sample.

## 5. Discussion and conclusions

In this paper, we have introduced and demonstrated an original method to measure broadband SRS spectra by using FT spectroscopy. The method profits from the ultrastable and reproducible positioning of the TWINS interferometer and from the noise reduction given by balanced detection and high-frequency lock-in modulation transfer, allowing to measure signals as small as  $1\div 3 \times 10^{-5}$ . We have applied the method to both spectroscopy –to measure the spectra of a series of solvents– and microscopy –to image and distinguish PMMA and PS spheres based on their Raman signatures.

FT spectroscopy is traditionally employed in the mid-IR range, where multichannel detectors are difficult and expensive. In this wavelength range, in addition, the sensitivity is limited by the detector noise and the use of a single detector provides an improvement with respect to a detector array (the so-called Fellgett's advantage [44]). In the visible/near-IR range, on the other hand, the sensitivity is limited by the laser intensity noise, so that Fellgett's advantage does not apply. Under these conditions, a multichannel detection, if available, would turn out to be advantageous with respect to a single channel FT detection, as extensively discussed in the context of optical coherence tomography [45,46]. However, it is currently technologically very challenging. In addition, for shorter wavelengths the demands on the stability of the interferometer become increasingly difficult to satisfy, making FT spectroscopy not very commonly used in the visible/near-IR range. Here we exploit on the one hand the very high accuracy and stability of TWINS to solve the problem of building a stable interferometer at short wavelengths; on the other hand, we use the FT approach to combine broadband acquisition with the sensitivity required for SRS imaging, which is typically achieved with a single-channel detection chain. Our method, which involves scanning of the interferometer for FT detection, is an elegant alternative to other approaches which scan the detuning of narrowband pump/Stokes pulses [20,21], the delay of broadband spectrally focused pump/Stokes pulses [30-32] or, possibly, the detected Stokes wavelength by a monochromator.

While this study provides a proof of concept of a new method for broadband SRS imaging, the current measurement time is too long for practical applications. The pixel dwell time in our case is limited to  $\approx 1\text{s}$ , which translates into several hours for a large image. There are, however, two strategies that, used in parallel, promise to decrease the measurement time by several orders of magnitude: (i) undersampling and (ii) step scanning. The former consists in sampling the interferogram at a frequency  $f_s$  lower than the Nyquist limit (corresponding to  $2f_H$ , where  $f_H$  is the highest optical frequency). Replicas of both Stokes and SRS spectra will appear in the FT of the interferogram at lower frequencies (called aliases) as mirror images of the original

spectra. A full recovery of the original spectrum is however still within reach, if replicas do not overlap each other. This may be obtained by a proper choice of  $f_s$  in a range that depends on both  $f_H$  and the bandwidth  $B$  of the optical signal, following the condition  $\frac{2f_H}{n} < f_s < \frac{2(f_H-B)}{n-1}$ , where  $n$  is an integer that represent the undersampling factor and that must reside in the range  $1 < n < \frac{f_H}{B}$ . In our case, since the overall Stokes spectrum extends approximately over 20% of the carrier frequency,  $n$  can be as high as  $\frac{f_H}{B} = \frac{1}{20\%} \sim 5$ , so that it is possible to undersample the interferogram at a frequency  $f_s$  that is  $\sim 5$  times lower than the Nyquist limit frequency  $2f_H$ . In our case, as we are only aiming at measuring the C-H lipid region of the Raman spectrum, which extends –at most– from  $f_L \approx 2750$  to  $f_H \approx 3150$   $\text{cm}^{-1}$ , we can push the downsampling approach up to almost  $n=8$ , meaning that we can acquire just one sample every 4 fringes. We applied this approach to the interferogram of Fig. 3(b), consisting of  $\sim 300$  fringes (blue solid curve). From the experimental interferogram we created a subset of the data, selecting one sample every 47, so that we reduced the amount of samples from the actual  $\approx 4000$  samples to just 85. The resulting interferogram is plotted in Fig. 3(b) as orange circles, corresponding to slightly more than one sample every 4 fringes. The FT of this undersampled subset (normalized with respect to the Stokes spectrum) is shown as an orange dashed line in Fig. 3(d). One can clearly see that it nicely follows the original SRS spectrum obtained with the full dataset (blue solid curve) with a very similar noise level, which means that our scan parameters were very conservative. This demonstrates the capability of the downsampling approach alone to reach acquisition speeds almost 50 times shorter, in the 20-ms range per spectrum.

The second ameliorative strategy can turn the possibility of an undersampled acquisition to a direct time gain. It consists in performing step-scan FT imaging. Thanks to the inherent stability and highly reproducible positioning of the TWINS interferometer, we could scan an entire line of the sample or even the whole image frame at a fixed delay, and then repeat the acquisition at various delays, thus computing the FT only at the end of the acquisition. This rapid raster scanning would have the additional advantage of reducing the pixel dwell time and thus the thermal load on the sample. We are currently limited to  $\approx 2.5$  mW pump power by the sample damage threshold. Increasing the pump power to the  $\approx 50$ -mW level, typically used in combination with fast sample scanning [21,25,29], would allow us to generate 20 times higher SRS signals, which would turn into a reduction of the integration time by a factor of about 100 while preserving the signal-to-noise ratio, thus allowing to collect broadband SRS images in a few seconds. We believe that the implementation of such strategies will make broadband FT-SRS of high interest for a wide range of applications in life sciences and material sciences.

### Acknowledgments

The research leading to these results has received funding from the European Research Council Consolidator Grant VIBRA (ERC-2014-CoG No. 648615) and Advanced Grant STRATUS (ERC-2011-AdG No. 291198) and from the project ‘Surface-enhanced Coherent Anti-Stokes Raman Scattering for Label-free Ultrasensitive Detection’ from Fondazione Cariplo (grant no. 2012-0904). JR thanks the Swiss National Science Foundation for financial support (Fellowship PBZHP2\_143444).